Draft version November 20, 2025
Typeset using LaTeX default style in AASTeX63

Advancing Identification method of Gamma-Ray Bursts with Data and Feature Enhancement

Peng Zhang (张鹏) [1,2] Bing Li (李兵) [2,3,4] Ren-Zhou Gui (桂任舟),[1] Shao-Lin Xiong (熊少林) [2]
Yu Wang (王瑜),[5,6,7] Shi-Jie Zheng (郑世杰),[2] Guang-Cheng Xiao (肖广成),[8] Xiao-Bo Li (李小波),[2]
Yue Huang (黄跃),[2] Chen-Wei Wang (王晨巍) [2] Jia-Cong Liu (刘佳聪) [2] Yan-Qiu Zhang (张艳秋) [2]
Wang-Chen Xue (薛王陈) [2] Chao Zheng (郑超) [2] and Yue Wang (王悦) [2]

[1]College of Electronic and Information Engineering, Tongji University, Shanghai 201804, China
[2]Key Laboratory of Particle Astrophysics, Chinese Academy of Sciences, Beijing 100049, China,
libing@ihep.ac.cn,rzgui@tongji.edu.cn,xiongsl@ihep.ac.cn
[3]School of Astronomy and Space Science, Nanjing University, Nanjing 210023, China
[4]Guangxi Key Laboratory for Relativistic Astrophysics, Nanning 530004, China
[5]ICRA, Dip. di Fisica, Sapienza Università di Roma, Piazzale Aldo Moro 5, I-00185 Roma, Italy
[6]ICRANet, Piazza della Repubblica 10, 65122 Pescara, Italy
[7]INAF – Osservatorio Astronomico d'Abruzzo, Via M. Maggini snc, I-64100, Teramo, Italy
[8]Department of Physics, Jinggangshan University, Jiangxi Province, Ji'an 343009, China

ABSTRACT

Gamma-ray bursts (GRBs) are challenging to identify due to their transient nature, complex temporal profiles, and limited observational datasets. We address this with a one-dimensional convolutional neural network integrated with an Adaptive Frequency Feature Enhancement module and physics-informed data augmentation. Our framework generates 100,000 synthetic GRB samples, expanding training data diversity and volume while preserving physical fidelity-especially for low-significance events. The model achieves 97.46% classification accuracy, outperforming all tested variants with conventional enhancement modules, highlighting enhanced domain-specific feature capture. Feature visualization shows model focuses on deep-seated morphological features and confirms the capability of extracting physically meaningful burst characteristics. Dimensionality reduction and clustering reveal GRBs with similar morphologies or progenitor origins cluster in the feature space, linking learned features to physical properties. This perhaps offers a novel diagnostic tool for identifying kilonova- and supernova-associated GRB candidates, establishing criteria to enhance multi-messenger early-warning systems. The framework aids current time-domain surveys, generalizes to other rare transients, and advances automated detection in large-volume observational data.

Keywords: Gamma-ray astronomy (628), Gamma-ray bursts (629), High energy astrophysics (739), Convolutional neural networks (1938), Dimensionality reduction(1943), Astronomy data analysis (1858)

1. INTRODUCTION

Gamma-ray bursts are among the most energetic phenomena in the universe, releasing enormous amounts of energy in the form of gamma rays over remarkably short time frames. Despite decades of remarkable progress in observations and theoretical investigations, their origins remain elusive (Zhang 2011; Kumar & Zhang 2015; Mészáros 2019; Pe'er 2024), making GRB identification and classification a critical focus of contemporary astrophysical research (Lü et al. 2010; Zhang et al. 2022; Sun et al. 2023; Wang et al. 2024). The rise of multi-messenger and multi-band astronomy further underscores the need for efficient GRB detection (Margutti & Chornock 2021; Rudolph et al. 2023): timely and accurate detection enables follow-up observations of afterglows, host galaxy localization, characterization of associated counterparts, and constraints on GRB intrinsic properties.

GRB light curves often exhibit irregular, multi-peaked structures that encode rich physical information about their outbursts. While traditional classification criteria (e.g., duration, hardness) have been widely adopted, emerging evidence highlights the need for additional discriminants to address the "iceberg effect"—a phenomenon where low-signal-to-noise ratio (low-SNR) GRBs are partially submerged in background noise, disproportionately impacting short-

duration events (Lü et al. 2014; Moss et al. 2022). Traditional burst search algorithms identify GRBs by detecting signals in multi-time-bin, multi-energy-band light curves where the SNR exceeds a predefined threshold above the background (Band 2002; Blackburn et al. 2013; Cai et al. 2021). However, these methods face significant challenges, including accurate background estimation and optimal threshold selection, limiting their effectiveness in identifying faint or complex GRB events. These limitations motivate the development of advanced techniques to enhance GRB detection and classification accuracy.

In recent years, machine learning (ML) has emerged as a experimental tool for GRB detection. For example, Abraham et al. (2021) developed an ML algorithm for automated detection of GRB-like events using AstroSat/CZTI data, combining density-based spatial clustering with dynamic time warping to demonstrate ML's versatility and robustness in GRB identification. Among ML architectures, convolutional neural networks (CNNs)—a specialized deep learning (DL) framework—excel in pattern recognition tasks (Alzubaidi et al. 2021; Taye 2023), and have driven a paradigm shift in astrophysical data analysis by autonomously extracting features from multi-dimensional, multi-modal datasets. In GRB research, CNN-based approaches have achieved notable successes. Parmiggiani et al. (2021) developed a real-time CNN pipeline for AGILE-GRID intensity maps, detecting 21 GRBs at 3σ significance compared to only two detections via conventional SNR-based searches. Parmiggiani et al. (2023) used a CNN autoencoder to reconstruct background light curves and identify 72 previously uncataloged AGILE GRBs. Additionally, (Parmiggiani et al. 2024) and Crupi et al. (2023) leveraged neural networks to predict background count rates and identify faint, long-duration GRBs.

Notably, GRB identification relies on extracting meaningful features from light curves with complex temporal and spectral characteristics. While traditional 1D-CNNs effectively capture local temporal patterns, their inability to model spectral-temporal correlations limits their utility in GRB analysis—critical GRB features are jointly encoded in both domains (Guidorzi et al. 2016; Tarnopolski & Marchenko 2021; Zhou et al. 2024). To address this, recent time series classification advances have introduced architectures that explicitly model frequency information, including Wavelet-based decomposition (e.g., T-WaveNet (Liu et al. 2020)), 2D temporal representations (e.g., TimesNet (Wu et al. 2022)), hybrid Fourier-wavelet transformers (e.g., FEDformer (Zhou et al. 2022), WFTNet (Liu et al. 2024)), and adaptive spectral blocks (e.g., TSLANet (Eldele et al. 2024)). These state-of-the-art approaches confirm that spectral-temporal modeling enhances feature extraction, underscoring the need for GRB identification methods that integrate both temporal dynamics and frequency-domain characteristics.

Complementary to classification, dimensionality reduction techniques have provided valuable insights into GRB diversity. For instance, Jespersen et al. (2020) used t-distributed stochastic neighbor embedding (t-SNE) to categorize Swift/BAT GRBs to separate supernova-associated and kilonova-associated GRBs into long and short categories. Garcia-Cifuentes et al. (2023) identified 7 new extended emission (EE) GRB candidates via dimensionality reduction. Zhu et al. (2024) and Negro et al. (2025) used Uniform Manifold Approximation and Projection (UMAP) or t-SNE to reveal GRB clusters that transcend traditional duration-based classification, including distinct subgroups of kilonova-related GRBs. Similarly, Chen et al. (2024) and Chen et al. (2025) demonstrated robust bimodal GRB clustering and refuted intermediate GRB classes using unsupervised ML and dimensionality reduction. Collectively, these studies highlight the utility of such techniques for analyzing burst similarities and refining classification schemes.

Despite these advances, DL models face critical limitations in GRB research. First, data scarcity persists: the largest available GRB dataset (Fermi/GBM, 3900 events) remains insufficient for robust DL training (Zhang et al. 2024), due to limited labeled observations, skewed distribution (underrepresentation of rare, short-duration, and low-SNR GRBs), and narrow coverage of physical properties (e.g., redshift, energy bands, progenitors). While data augmentation has been explored to mitigate this (Zhang et al. 2024; Shorten & Khoshgoftaar 2019), existing datasets still lack the feature richness needed to avoid overfitting. Second, uncertainty quantification (UQ) is underdeveloped: model uncertainty stems from limited training data, the "black-box" nature of CNNs, and observational noise (Nemani et al. 2023), yet UQ is critical for distinguishing high-confidence detections from ambiguous candidates—misclassification of which could lead to missed follow-up observations or erroneous inferences about progenitor origins.

To address these limitations, we present an integrated framework that combines physics-informed data augmentation (to enhance sample diversity) with a novel frequency-adaptive feature enhancement module (to capture spectral-temporal correlations). In this Letter, Section 2 details data preprocessing, augmentation, and dataset construction. Section 3 describes the model architecture, feature enhancement modules, training process, and feature analysis framework. Section 4 presents performance metrics and classification results, and Section 5 discusses the implications of our approach and summarizes conclusions.

2. DATA AUGMENTATION AND DATASET

The Fermi/GBM trigger system has been operational since 12 July 2008 (first detected GRB: GRB 080714B). For this study, we utilized Fermi/GBM data spanning from 14 July 2008 to 30 June 2024, including 3,905 original GRBs detected by NaI detectors. These events are manually verified and cataloged in the Fermi/GBM Burst Catalog[1]. Adopting the GRB/non-GRB extraction protocol described in Zhang et al. (2024), we updated the dataset by segmenting samples into 120-second time windows. To ensure complete coverage of the T_{90} interval (with background included on both sides), 217 GRBs failing this criterion were excluded. For the remaining events, samples were generated based on the number of triggering NaI detectors, resulting in 6,189 primary GRB samples. Non-GRB samples—encompassing modulated background, electronic noise, and potential all-sky source signals—were systematically extracted from detectors' quiescent (non-trigger) intervals, totaling 108,000. This balance between classes enhances model generalization to non-burst events.

Light curves for all samples were extracted at a 64 ms temporal resolution across 128 energy channels, then rebinned into 9 standard energy bands (25–50, 50–100, 50–300, 100–300, 100–500, 100–900, 300–500, 300–900, 500–900 keV). This segmentation aligns with typical GRB photon energy distributions and Fermi/GBM trigger criteria (von Kienlin et al. 2020; Cai et al. 2021), approximating the photon deposition ranges of NaI detectors (without energy response correction). Critically, it preserves energy-dependent features such as burst morphology evolution, light curve shape variations, and spectral lags—enriching the diversity of discriminative features for model training. To optimize input for machine learning, we applied per-band standardization to light curves (scaling features to zero mean and unit variance). This approach preserves spectral information via inter-band flux ratios, empirically outperforming normalization (scaling to [0,1]). While both methods unify feature scales to facilitate deep learning convergence, standardization is preferable for GRB characterization as it retains spectral integrity—essential for distinguishing GRBs from non-GRBs (e.g., via hardness evolution or spectral lags).

Data augmentation: We first compute the full-energy band peak signal-to-noise ratio (peak-SNR) of primary GRB samples and fit its distribution using a log-normal function. This fitted distribution is then used for random sampling to generate more synthetic GRB samples. Specifically, we randomly reduce the count rate of original GRB light curves multiple times. For each GRB, a single reduction factor is applied to all its 9 energy band light curves in each reduction, generating distinct light curves with unique SNRs—effectively enhancing training set diversity. For instance, as illustrated in Figure 1, we generated three synthetic light curves (distinct SNRs) for GRB 230307A. This approach is analogous to resizing or contrast enhancement in affine data augmentation.

Given an input light curve $\mathbf{LC} \in \mathbb{R}^T$ ($\mathbb{R}$: real numbers; T: temporal length) and a background light curve $\mathbf{LC}_{bg} \in \mathbb{R}^T$, the augmented light curve $\mathbf{LC}_{new}$ is computed as:

$$\mathbf{LC}_{new} = \mathbf{LC} \cdot (1 - \alpha) + \text{Poisson}(\mathbf{LC}_{bg} \cdot \alpha), \tag{1}$$

where $\alpha \in [0, 1]$ is the *crop factor* controlling burst photon deduction proportion. The Poisson($\cdot$) function introduces stochastic noise, restoring matching Poisson-distributed background noise to simulate real astronomical random noise. This formula reduces burst signal significance while preserving original background levels, ensuring synthetic samples match real scenarios (e.g., orbit modulation, instrument noise). Notably, this method reproduces different degrees of the "iceberg effect" in synthetic GRBs—especially effective for enriching short-duration, rare faint, and low-SNR GRB samples. Crucially, augmented samples faithfully retain inherent fine-scale temporal/ spectral substructures of original GRBs, ensuring no excessive loss of key physical features for GRB identification/classification. The data augmentation process is detailed below, with statistical results shown in Figure 2:

1. Analyze full-energy band peak-SNR of 6,189 primary GRB samples and fit this distribution with a log-normal function over [0,25] σ.

2. Randomly sample 500,000 values from the fitted distribution and divide by 25 to scale [0,25] σ to [0,1], yielding *crop factors* (α).

3. Uniformly sample 500,000 instances from primary GRB samples and pair each with a random α, then generate 500,000 synthetic samples via Equ. 1. Use the same α for all 9 energy bands of a GRB to preserve spectral consistency.

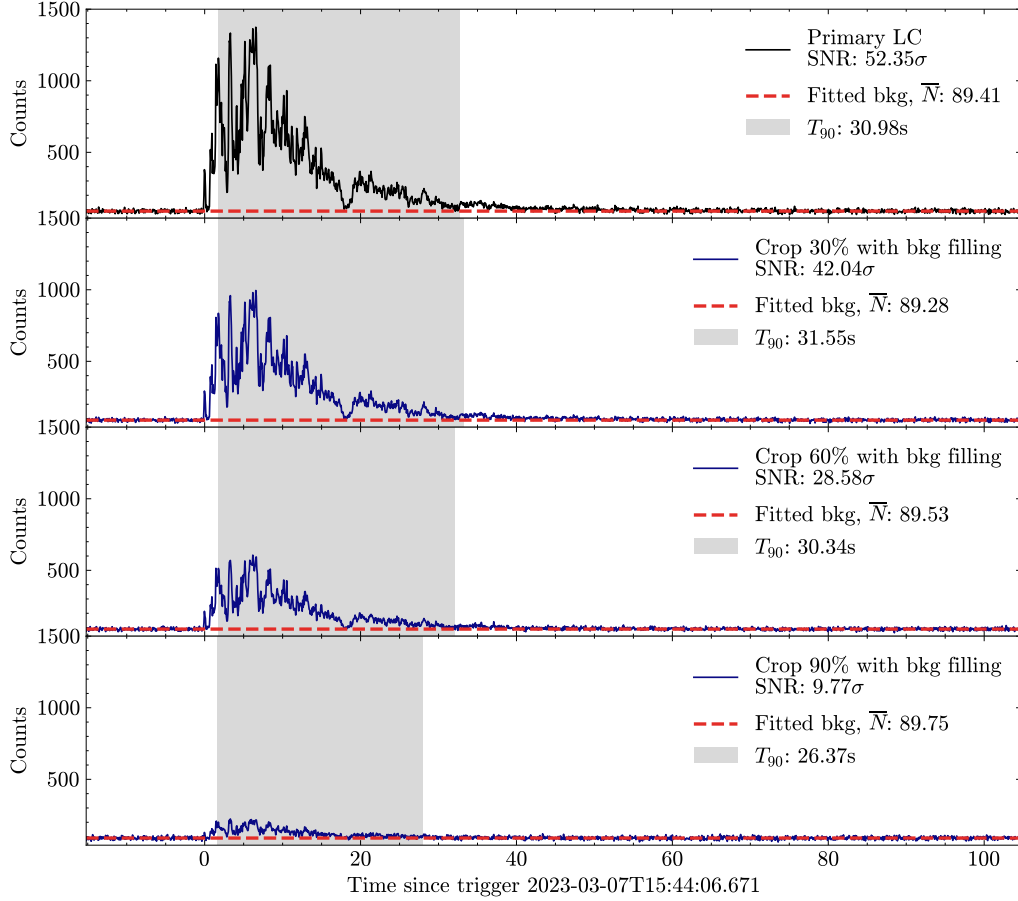[1] https://heasarc.gsfc.nasa.gov/W3Browse/fermi/fermigbrst.html

Figure 1. Data augmentation procedure for GRB light curves, using GRB 230307A as observed by Fermi/GBM detector n8 (full energy channel). The top panel presents the original light curve with a peak-SNR of $52.35\,\sigma$, where the red dashed line indicates the polynomial-fitted background level (mean count rate ~ 90 counts/bin) and the shaded area marks the T_{90} interval. The lower panels show the resulting light curves after applying count rate reductions of 30%, 60%, and 90% to each time bin, with subsequent restoration of Poisson-distributed background noise at the corresponding levels. The resulting peak SNR values are indicated for each modified light curve.

4. Remove 4,648 synthetic samples with peak-SNR blew $2\,\sigma$, as excessive photon subtraction makes these resemble background samples.

5. Randomly draw 100,000 samples from the remainder to balance GRB/non-GRB ratios in the training set[2].

6. Apply the same augmentation to non-GRB samples to align background noise distributions, ensuring the model distinguishes GRBs from background (not artificial Poisson noise differences).

Dataset: We partition preprocessed samples into training, validation, and test sets chronologically to ensure temporal generalization. Dataset details are shown in Table 1. This chronological split alleviates temporal overfitting while preserving the data's inherent flux distribution. We maintain $\sim$ 1:1 positive-to-negative sample ratios across all splits. Crucially, only the training set undergoes data augmentation, validation/test sets retain original observations (primary GRB samples and non-GRB samples) for unbiased performance evaluation.

3. MODEL ARCHITECTURE, TRAINING, AND EXTENSION

3.1. *Architecture of Neural Networks*

---

[2] For this supervised task, final sample size was determined via prior experience with similar models, relying on empirical heuristics.
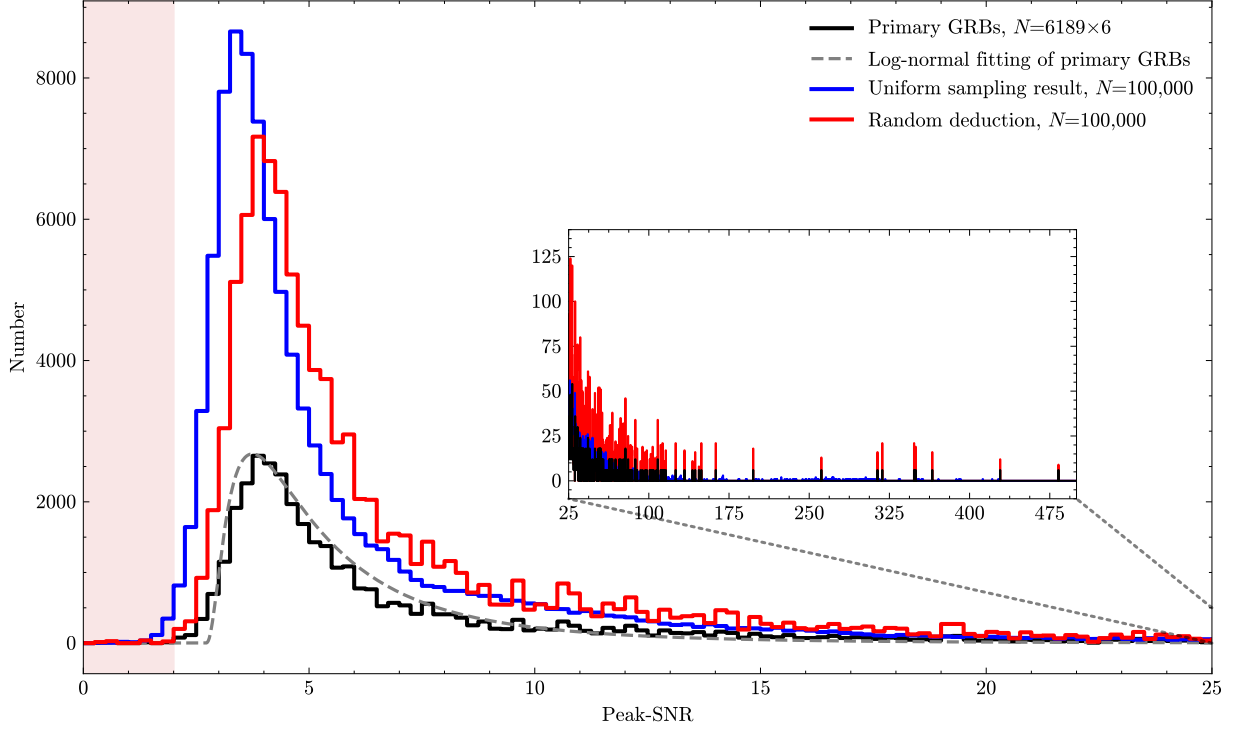
Figure 2. Histogram of full-energy band peak-SNRs for GRB samples during the data augmentation process. The solid black line represents the SNR distribution of the primary sample, scaled by a factor of 6 for visualization. The dashed gray line denotes the fitted log-normal distribution over the range $[0, 25]\,\sigma$. The solid blue line shows the peak-SNR distribution of 100,000 uniformly sampled instances from the primary GRB samples. The solid red line represents the peak-SNR distribution of 100,000 randomly selected GRB samples after data augmentation The pink shaded area highlights peak-SNR values below $2\,\sigma$.

Table 1. Description of the dataset.

Dataset	Nu. of GRB Events		Nu. of Samples		Period Definition (UTC)
	Original GRBs	Primary GRBs	Synthetic GRBs	Non-GRBs	
Training set	1,899	6189	100,000	100,000	07/14/2008 - 31/12/2016
Validation set	842	2,774	2,774	4,000	01/01/2017 - 12/31/2019
Test set	947	3,143	3,143	4,000	01/01/2020 - 06/31/2024

Each sample in our dataset consists of light curves spanning 9 energy bands, which are naturally suited to be treated as time series data. This makes a 1D CNN the appropriate choice for feature extraction and classification. Our model adopts ResNet (He et al. 2016) as its backbone, which relies on a sequential stack of four convolutional units (Conv Units) to progressively extract hierarchical features from the input light curves. A key advantage of ResNet is its integration of residual connections, which effectively alleviate the gradient vanishing problem that commonly arises in deep neural networks and enable stable training of deeper architectures. To address the limitation that CNNs lack the ability to distinguish subtle frequency variations, we propose an Adaptive Frequency Feature Enhancement module, AFFE, which is integrated into the last part of each Conv Unit. This module explicitly enhances frequency-domain features to improve the model's GRB identification capability, and it also adaptively weights and filters frequency components, enabling the model to focus on the most discriminative features for GRB recognition. This design is particularly critical for distinguishing GRBs from background noise, as frequency-domain analysis can uncover patterns that remain obscured in the time domain.

After the convolutional layers (including Conv Units with AFFE modules) complete feature extraction, the extracted high-dimensional features first undergo global average pooling (GAP). This step reduces the number of model parameters while preserving the representative information of features across the temporal dimension, thereby mitigating the risk of overfitting. A dropout layer with a 50% dropout rate is then inserted between the GAP layer and the subsequent fully connected (FC) layers. During training, this layer randomly deactivates half of the neurons to prevent the model from over-relying on specific features, further suppressing overfitting. Following the dropout layer, two FC layers map the pooled features to the final classification space and output the probability of the sample belonging to the GRB or non-GRB category. The overall architecture of our our ResNet-based model integrated with AFFE modules is shown in Figure 3, which includes the order of layers and the data flow.
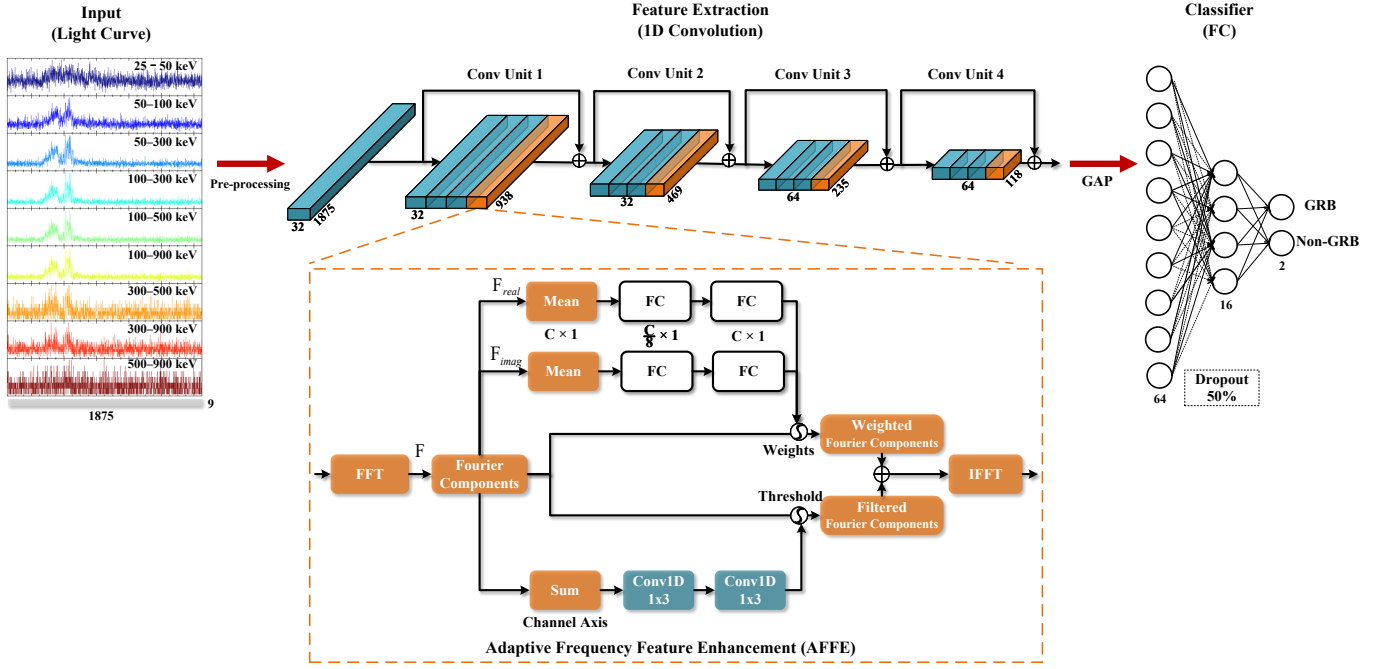

Figure 3. Schematic diagram of the ResNet+AFFE model architecture and the feature transformation process across layers. The input light curves are colored differently to distinguish the nine energy bands (This color distinction is solely for intuitively distinguishing each energy band to improve the clarity of the diagram, with no additional physical implications.). The numbers inside each Conv unit indicate changes in feature map size and channel dimension. The yellow modules represent the AFFE modules, and the dashed box at the bottom details an implementation of the AFFE module.

Here we describe the AFFE module in detail. Given an input feature map $\mathbf{X} \in \mathbb{R}^{T \times C}$ (with T as temporal length and C as channel number), the AFFE module processes it in the following steps:

1. **Frequency Transformation**: The input feature map $\mathbf{X}$ is first transformed into the frequency domain using the Fast Fourier Transform (FFT):

$$\mathbf{F} = \text{FFT}(\mathbf{X}), \tag{2}$$

where $\mathbf{F} \in \mathbb{C}^{T \times C}$ denotes the complex-valued Fourier frequency spectrum. The real and imaginary parts of $\mathbf{F}$ are denoted as $\mathbf{F}_{\text{real}}$ and $\mathbf{F}_{\text{imag}}$, respectively.

2. **Weighted Frequency**: To adaptively emphasize important frequency components, we apply separate learnable transformations to the real and imaginary parts of the frequency spectrum. Specifically, four FC layers are used to generate adaptive weights for $\mathbf{F}_{\text{real}}$ and $\mathbf{F}_{\text{imag}}$:

$$\mathbf{W}_{\text{real}} = \text{FC}_2(\text{FC}_1(\mathbf{F}_{\text{real}})), \quad \mathbf{W}_{\text{imag}} = \text{FC}_4(\text{FC}_3(\mathbf{F}_{\text{imag}})), \tag{3}$$

where $\mathbf{W}_{\text{real}}, \mathbf{W}_{\text{imag}} \in \mathbb{R}^{T \times C}$ are the learned weight matrices. The number of neurons in the FC_1 and FC_3 is set to C divided by 8. This choice is determined after comparing division factors of 2, 4, 8, and 16, and it

significantly reduces the parameter count of the module. The weighted frequency spectrum is then computed as:

$$\mathbf{F}_{\text{weighted}} = \mathbf{W}_{\text{real}} \odot \mathbf{F}_{\text{real}} + i \cdot (\mathbf{W}_{\text{imag}} \odot \mathbf{F}_{\text{imag}}), \tag{4}$$

where $\odot$ denotes element-wise multiplication.

3. **Filtered Frequency**: To further refine frequency features, we perform a filtering operation in the frequency domain. First, the weighted frequency spectrum $\mathbf{F}_{\text{weighted}}$ is summed along the channel dimension to obtain a channel-aggregated frequency representation $\mathbf{F}_{\text{sum}} \in \mathbb{C}^{T \times 1}$. Two one-dimensional convolutional layers are then applied to $\mathbf{F}_{\text{sum}}$ to learn a frequency thresholding function that approximates a low-pass filter:

$$\mathbf{F}_{\text{filtered}} = \text{Conv}_1(\text{Conv}_2(\mathbf{F}_{\text{sum}})). \tag{5}$$

The filtered spectrum $\mathbf{F}_{\text{filtered}}$ is then broadcasted back to the original channel dimension.

4. **Frequency Feature Fusion**: The results of the Weighted Frequency and Filtered Frequency steps are combined through element-wise addition:

$$\mathbf{F}_{\text{enhanced}} = \mathbf{F} \odot \mathbf{F}_{\text{weighted}} + \mathbf{F} \odot \mathbf{F}_{\text{filtered}}. \tag{6}$$

5. **Inverse Transformation**: Finally, the enhanced frequency spectrum $\mathbf{F}_{\text{enhanced}}$ is transformed back to the time domain using the Inverse Fast Fourier Transform (IFFT):

$$\mathbf{X}_{\text{enhanced}} = \text{IFFT}(\mathbf{F}_{\text{enhanced}}), \tag{7}$$

where $\mathbf{X}_{\text{enhanced}} \in \mathbb{R}^{T \times C}$ is the output feature map with enriched frequency-domain information.

3.2. *Model training and analysis*

Model parameters are initialized using the truncated normal distribution proposed by He et al. (2015). A detailed analysis of hyperparameter choices-including batch size, learning rate, and number of convolutional layers-is conducted to evaluate their impact on the test set, following the approach in Ma et al. (2023). Further details on hyperparameter selection, such as the number of convolutional kernels per unit, convolutional kernel sizes, and neuron counts in FC layers. The training configuration is as follows: batch size is set to 1024; cross-entropy loss is used to measure the discrepancy between predicted and true labels; and the Adam optimizer Kingma & Ba (2014) is adopted to dynamically update model parameters and minimize loss during training. The initial learning rate is 1×10^{-4}, with a scheduling mechanism that reduces the rate by half if validation loss does not decrease for 10 consecutive epochs. To prevent overfitting, early stopping terminates training if validation accuracy plateaus for 20 consecutive epochs. The patience value was selected after testing ranges of [10, 20, 40] epochs, and the model parameters from the epoch with the highest validation accuracy are retained as the final optimal parameters. The result of the optimizing choices are highlighted in bold in Table 2. The efficacy of selected hyperparameters is further validated by training curves, which demonstrate stable convergence and appropriate model capacity for the classification task.

We conducted a comparative analysis involving the baseline ResNet architecture that commonly used for time series data, and ResNet variants integrated with existing feature enhancement modules that including the SE (Squeeze-and-Excitation block; Hu et al. (2018)), CBAM (Convolutional Block Attention Module; Woo et al. (2018)), ECA (Efficient Channel Attention module; Wang et al. (2020)), and ASB (Adaptive Spectral Block; Eldele et al. (2024) modules), and our proposed ResNet-AFFE model. All models were trained and tested on our dataset using hyperparameters consistent with those reported in the original literature for each comparative module. This ensures a fair performance comparison, and the results of this comparison (for ResNet variants and our ResNet-AFFE model) on the test set are presented blew.

The models were implemented using the PyTorch framework, with training conducted on a single NVIDIA RTX-4090 GPU. Performance was evaluated using four standard classification metrics: *Accuracy*, *Precision*, *Recall*, and *F1-score*, consistent with the evaluation methodology reported in Zhang et al. (2024). Accurately verifying these metrics and their associated prediction uncertainties is critical, as they quantify confidence in model predictions and provide a scientific basis for subsequent decision-making. During testing, we achieved robust uncertainty quantification for deep learning predictions via Monte Carlo Dropout (MCD, for references see Gal & Ghahramani (2015); Basora

Table 2. Hyper-parameter selection.

Parameters	Values
Number of ConvUnit	2, **4**, 8, 16
Number of Conv in ConvUnit	1, 2, **3**, 4
First ConvUnit filter size	16, **32**, 64, 128, 256, 512
Second ConvUnit filter size	16, **32**, 64, 128, 256, 512
Third ConvUnit filter size	16, 32, **64**, 128, 256, 512
Fourth ConvUnit filter size	16, 32, **64**, 128, 256, 512
Norm function after Conv	InstaceNorm, **BatchNorm**
Activation function	Sigmoid, **Relu**
FC neurons	8, 16, 32, **64**, 128
Dropout rate	0.3, **0.5**, 0.8
Initial learning rate	1e-3, **1e-4**, 1e-5, 1e-6
Batch size	512, **1024**, 2048
Patience of reduce learning rate	5, **10**, 15

NOTE—Bold text represents that the model performs optimally on that metric.

et al. (2025)). In this procedure, all model parameters are kept fixed, and dropout layers between FC layers remain activated. For each forward pass, the dropout rate is randomly sampled from a uniform distribution over the interval [0.1, 0.5]. This stochastic forward pass is repeated 1000 times, which allows computation of the mean and standard deviation for each metric—thereby effectively estimating predictive uncertainty. The performance and uncertainty of all models are summarized in Table 3.

Table 3. Comparison of models' performance on test set.

Model	*Accuracy* (%)	*Precision* (%)	*Recall* (%)	*F1-score* (%)
ResNet	97.17 ± 0.13	98.80 ± 0.14	94.71 ± 0.20	96.72 ± 0.15
ResNet+SE[a]	97.33 ± 0.04	99.08 ± 0.05	94.82 ± 0.08	96.90 ± 0.04
ResNet+CBAM[b]	97.29 ± 0.07	99.08 ± 0.08	94.72 ± 0.14	96.85 ± 0.09
ResNet+ECA[c]	97.34 ± 0.07	99.15 ± 0.08	94.76 ± 0.13	96.91 ± 0.08
ResNet+ASB[d]	97.40 ± 0.07	99.24 ± 0.08	$\mathbf{94.83 \pm 0.14}$	96.98 ± 0.09
ResNet+AFFE (Ours)	$\mathbf{97.46 \pm 0.07}$	$\mathbf{99.39 \pm 0.07}$	94.81 ± 0.14	$\mathbf{97.04 \pm 0.08}$

NOTE— The uncertainty of each metric is evaluated utilizing MCD. Bold text represents that the model performs optimally on that metric.
Enhanced time domain feature extraction module: [a] Hu et al. (2018), [b] Woo et al. (2018), [c] Wang et al. (2020).
Enhanced frequency domain feature extraction module: [d] Eldele et al. (2024).

To examine whether ResNet-AFFE prioritizes burst-specific temporal signatures (e.g., T_{90} intervals or energy-dependent flux peaks) over noise, we used Gradient-weighted Class Activation Mapping (Grad-CAM)—a mainstream visualization technique for addressing deep learning's "black box" problem. Grad-CAM generates gradient-weighted heatmaps to identify features most influential to model predictions (Selvaraju et al. 2017), enhancing interpretability. For time-series light curves, these heatmaps pinpoint temporal segments driving classification outputs, replacing ambiguous "feature importance" with intuitive visual evidence. We employ Grad-CAM to decode our model's decision-making process for GRB classification. Comparative visualizations of discriminative temporal features between the baseline ResNet and ResNet-AFFE are presented in Figure 4.
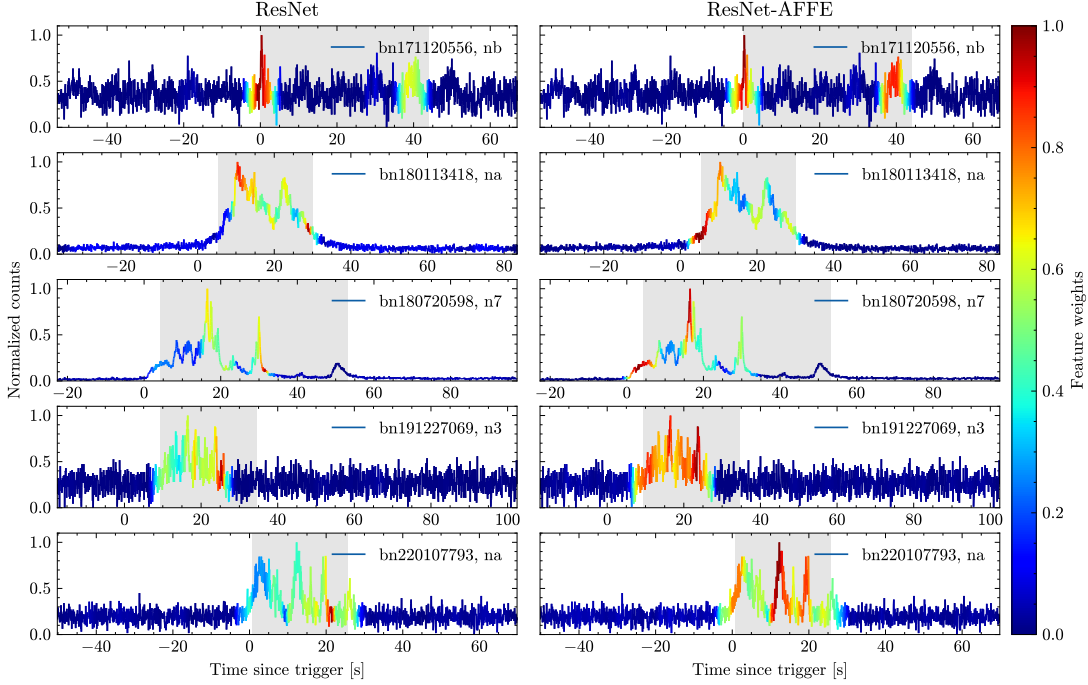
Figure 4. Feature visualization for five representative GRBs using Grad-CAM. The color-coded heatmaps indicate the temporal regions receiving strongest attention from the deep learning model during classification. Left and right panels contrast the feature extraction patterns between the ResNet (left) and our enhanced ResNet-AFFE architecture (right). Gray shaded regions denote the T_{90} for each GRB.

We further mapped deep features extracted by ResNet-AFFE to observed physical characteristics using UMAP, a nonlinear dimensionality reduction method rooted in graph theory and manifold learning that effectively projects high-dimensional data to low-dimensional spaces for structural analysis. We analyzed 3,833 GRBs detected by Fermi/GBM over the period 2008–2024, concatenating light curves from the triggering detectors of each GRB as model input. Notably, our model uses GAP to aggregate features from the last convolutional layer, enabling compatibility with variable-length data under uniform batch input. This design specifically supports the inclusion of long GRBs with $T_{90} >$ 120 s, which would otherwise be excluded by fixed-length constraints. UMAP takes as input the output results from the last convolutional layer of ResNet-AFFE and outputs 2D projections that uncover intrinsic correlations of features between GRBs. Key UMAP hyperparameters including $n\_neighbors$ and min_dist were systematically optimized via exhaustive parameter space exploration (over ranges: $2 \leq n\_neighbors \leq 100$; $0.01 \leq min\_dist \leq$ 0.99). Manual validation yielded optimal values of $n\_neighbors = 60$ and $min\_dist = 0.66$, achieving a balanced preservation of both global data structure and local neighborhood fidelity—two core advantages of UMAP in high-dimensional signal analysis. The resulting projections shown in Figure 5, visualize the distribution of true positive (TP) and false negative (FN) GRBs, with each GRB's peak-SNR and T_{90} encoded directly in the projection to link low-dimensional structure with physical observables. While UMAP effectively reveals the structure of high-dimensional data, its visualization results are sensitive to hyperparameter selection (e.g., $n\_neighbors$ and min_dist). To mitigate the subjectivity introduced by manual parameter tuning and ensure the robustness of observed clustering patterns, we implemented a cross-validation procedure.

Following the approach in Dimple et al. (2023), which targets latent clustering patterns in transient burst events, we further employed the AutoGMM module (Athey et al. 2019) to cluster features extracted by the ResNet-AFFE model. AutoGMM is an automated clustering tool that leverages Gaussian Mixture Models (GMMs) to infer the optimal number of clusters, and it assumes data points arise from a mixture of multiple Gaussian distributions, aligning with the statistical properties of GRB feature distributions. The algorithm first performs GMM clustering over a range of candidate cluster counts, then infers the Gaussian distribution parameters and cluster assignments that best fit the data—eliminating subjective manual cluster number selection. The four clusters identified via AutoGMM were visually distinguished using distinct color mappings in the UMAP projections, and their corresponding representative light
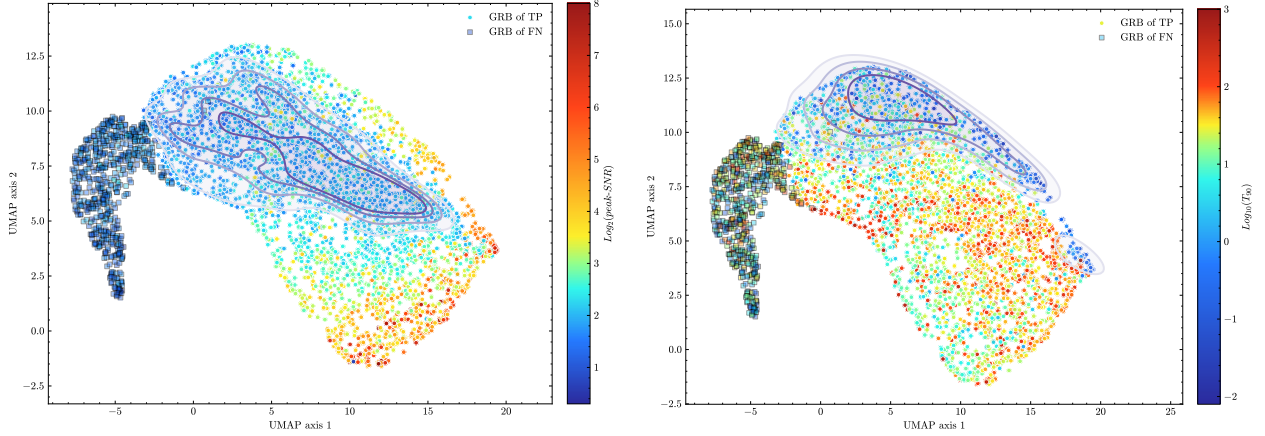
Figure 5. UMAP visualization of feature space representations extracted from the final convolutional layer of the ResNet-AFFE model. (Left) Points are color-coded according to $\log_2$(peak-SNR) values for individual GRBs. The purple contour represents the kernel density estimate (KDE) of low-significance TP events (peak-SNR $< 5\sigma$). (Right) Points are color-coded according to $\log_{10}(T_{90})$ values from the *Fermi* burst catalog. The purple contour shows the KDE of short-duration TP events ($T_{90} < 2\,\mathrm{s}$).

curves were presented around, as shown in Figure 6. Figure 7 further delineates the spatial distribution of physically distinct GRB subgroups and their proportions within each cluster, including kilonova-associated GRBs (GRB-KN), supernova-associated GRBs (GRB-SN), extended-emission GRBs (GRB-EE), ultra-long GRBs, and short/long GRBs with precursors.

4. RESULT

All datasets used in this study are derived from Fermi/GBM observational data, divided into three defined subsets for training, validation, and testing. The training set incorporates synthetic GRB samples generated via our proposed data augmentation technique, designed to increase sample size and enhance the diversity of burst signals. The efficacy of this method is visually validated in Figure 1, which illustrates controlled modulation of burst SNR while preserving background levels. Focused on sampling and attenuation factors, the augmentation notably enriches low-SNR GRB representation: as shown in Figure 2, the peak-SNR distribution of GRB samples expands toward lower values, increasing total GRB training samples from 6,189 to over 100,000. Non-GRB samples—sourced from triggerless time-tagged event (TTE) data—were similarly augmented to 100,000, ensuring class balance. For validation and testing, we used 2,774 and 3,143 primary GRBs, respectively, selected based on the number of triggering NaI detectors. Detailed dataset specifications are provided in Table 1. Each input sample consists of light curves across 9 energy bands (64 ms temporal resolution; Figure 3, left), with per-band standardization applied to reduce energy-specific magnitude biases. This preprocessing preserved fine-grained features, enhanced the model's feature extraction and generalization capabilities, and facilitated subsequent visualization analyses.

Our proposed classification framework employs a ResNet-based 1D-CNN within a supervised learning paradigm, designed for binary classification (GRB vs. non-GRB). Its core capability lies in extracting discriminative features from multidimensional data and differentiating classes based on these features. The complete model architecture—incorporating the novel AFFE module—is shown in Figure 3. The AFFE module employs a dual-path filtering architecture (Equation 6): the term $\mathbf{F} \odot \mathbf{F}_{\text{weighted}}$ performs frequency-adaptive soft-threshold denoising, while $\mathbf{F} \odot \mathbf{F}_{\text{filtered}}$ implements coherent feature extraction via an optimized matched-filter scheme. This integrated approach enables adaptive frequency selection without manual filter design, achieving simultaneous noise suppression and signal enhancement through data-driven spectral weighting. By weighting and filtering frequency-domain differences between GRBs and non-GRBs, the module optimizes extraction of discriminative features critical for classification.

Model parameters were optimized via backpropagation and gradient-based methods on our large-scale datasets, enhancing autonomous learning of salient features. Systematic evaluation of hyperparameter configurations identified the optimal set (Table 2). Training and validation loss curves reflect stable dynamics: the early stopping mechanism terminated training at epoch 18 (the optimal point), preserving parameters that generalize best to unseen data. Convergence of both curves—with no divergence between training and validation losses—confirms robust performance
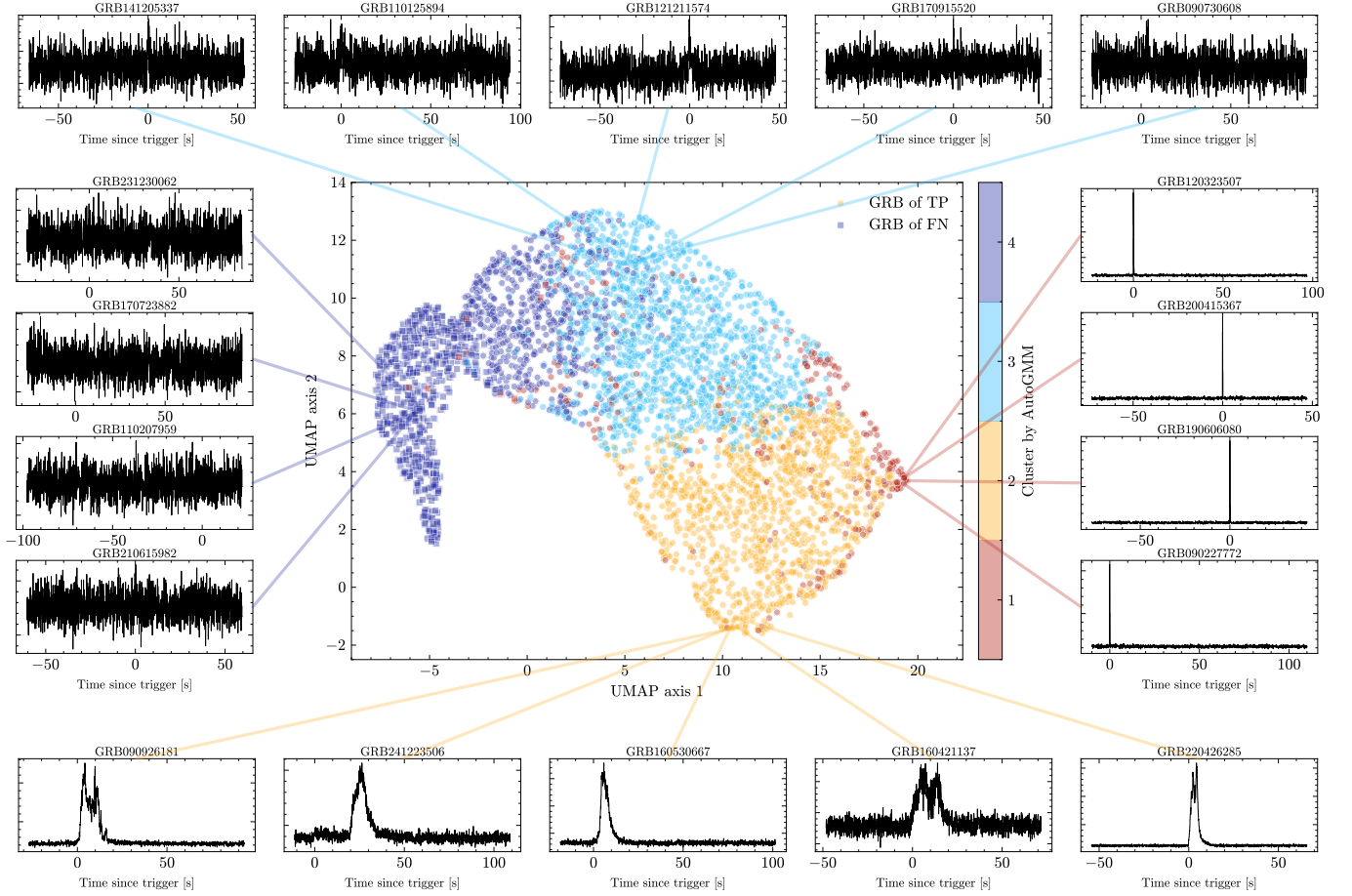
Figure 6. The dimensionality reduction results of UMAP algorithm for the output features of the last convolution layer of the ResNet-AFFE model, colored by their AutoGMM cluster assignments (four clusters). Surrounding panels display the full-band light curves of representative GRBs from each cluster.

without overfitting. We conducted a comparative analysis of multiple models on the test set, including: a baseline ResNet, ResNet variants with existing feature enhancement modules (SE, CBAM, ECA, ASB), and our ResNet-AFFE. All models were trained with hyperparameters consistent with their original literature to ensure fairness, and prediction confidence was estimated via Monte Carlo Dropout (1000 stochastic forward passes). Performance metrics and uncertainties are summarized in Table 3. Incorporating the AFFE module yielded a statistically quantifiable improvement in classification accuracy. Specifically, ResNet-AFFE achieved 97.46% accuracy—outperforming all tested variants with conventional enhancement modules—with consistent results across multiple experimental runs. Grad-CAM visualized the model's decision-making process, revealing that ResNet-AFFE prioritizes physically meaningful GRB characteristics. As shown in Figure 4, compared to the baseline ResNet, our model's attention is more strongly concentrated in the T_{90} interval (containing key prompt emission information) rather than random noise—highlighting a critical difference in feature focus. This visualization enables even untrained users to distinguish model robustness, even for identical predictions.

We applied UMAP to reduce the dimensionality of features from the last convolutional layer of ResNet-AFFE, using 3,833 original GRBs as input. Figure 5 presents the 2D projection, encoded with individual GRBs' peak-SNR and T_{90} values, revealing distinct clustering patterns: true positive (TP) and false negative (FN) GRBs occupy entirely separate regions. Of these GRBs, 593 were classified as FNs—99% with peak-SNR below 5σ and most being short-duration events. Dimensionality reduction further uncovered organized spatial distributions: low-SNR GRBs clustered in the upper-left region, while short-duration GRBs formed a narrow band along the upper-right edge, exhibiting a characteristic nonlinear distribution. Notably, GRBs with similar durations or SNRs showed discernible aggregation. Automated clustering via AutoGMM identified four distinct clusters from the features extracted by the ResNet-AFFE
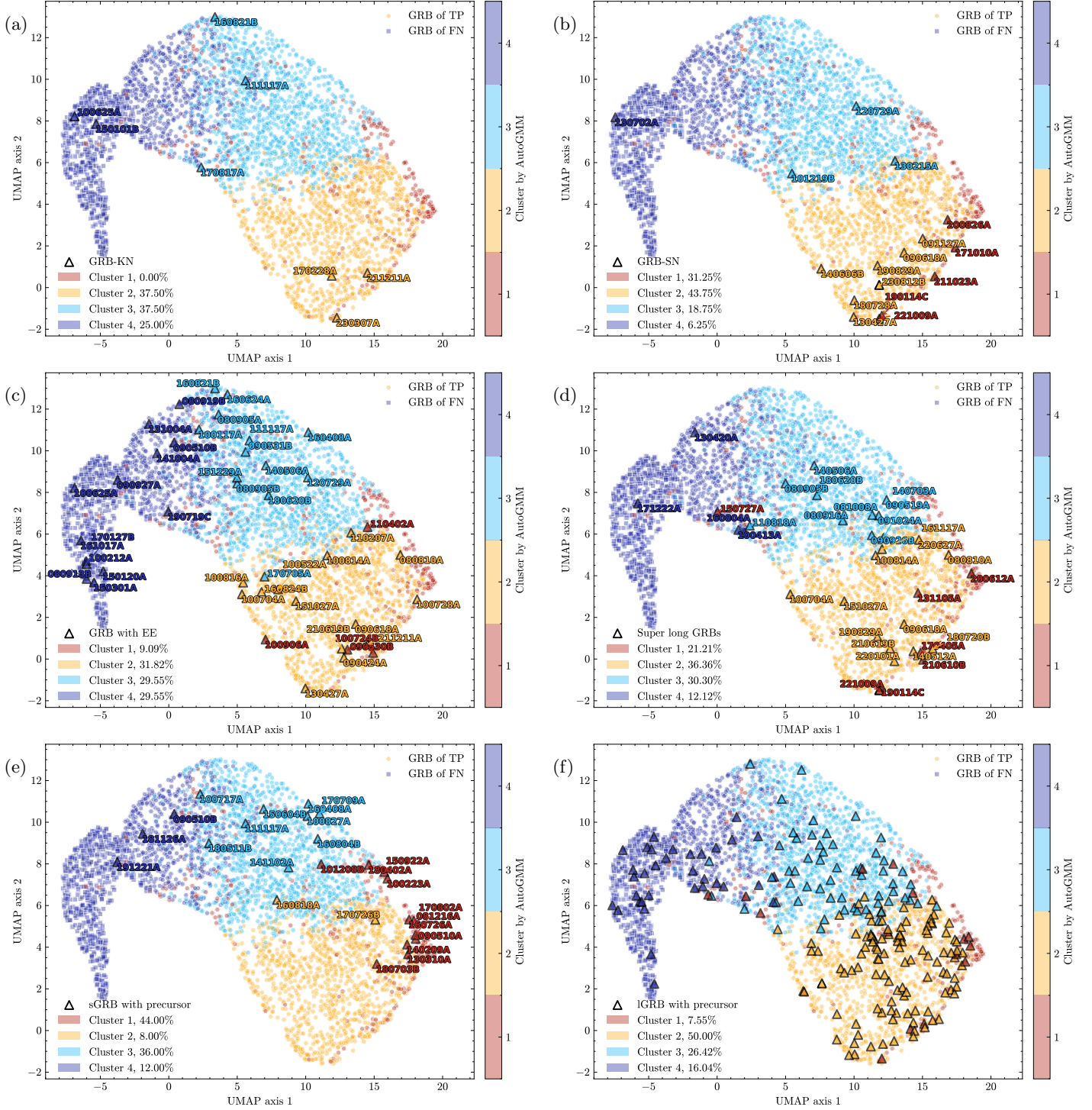
Figure 7. The dimensionality reduction results of UMAP algorithm for the output features of the last convolution layer of the ResNet-AFFE model, colored by their AutoGMM cluster assignments (four clusters). The triangular symbols in each sub-graph are the same series of GRBs detected by Fermi/GBM: (*a*) Kilonova-associated GRBs (GRB-KN, Li et al. (2023)), (*b*) Supernova-associated GRBs (GRB-SN) come from the GRBSN webtool (Finneran et al. 2024), (*c*) GRBs with extended emission (GRB with EE, Garcia-Cifuentes et al. (2023); Li et al. (2024)), (*d*) Super long GRBs (Ror et al. 2024), (*e*) Short GRBs with precursor (Zhong et al. 2019; Wang et al. 2020), (*f*) Long GRBs with precursor (Coppin et al. 2020; Deng et al. 2024).

model eliminating subjective manual selection. Figure 6 illustrates representative light curves for each cluster, mapped onto the UMAP-reduced space, directly linking clustering results to observable temporal morphology of GRBs. To further explore the physical relevance of clustering, we analyzed correlations between model-extracted features and GRBs of specific origins or morphologies, quantifying the proportion of these GRBs in each cluster to preliminarily assess associations. Figure 7 highlights these special GRBs in the dimensionality reduction projection: Kilonova-associated GRBs are predominantly localized within Clusters 2 and 3, while supernova-associated events are primarily concentrated in Clusters 1 and 2. GRBs with extended emission are uniformly distributed across Clusters 2 to 4. Ultra-long GRBs are spatially confined to the lGRB-dominated Cluster 3, suggesting distinct feature space signatures. Short GRBs with precursors exhibit a concentrated spatial distribution within Cluster 1, occupying both peripheral regions and transitional zones bridging short and long GRB populations. Long GRBs with precursors contrastingly show half their population concentrated in Cluster 2 with uniform dispersion. This visualization reveals natural separations in the learned feature space between GRBs of different physical origins.

5. DISCUSSION AND CONCLUSION

This study develops an integrated deep learning framework for high-precision GRB identification, addressing core challenges in transient astrophysical event detection through targeted methodological innovations. The transient nature of GRBs poses a fundamental obstacle to deep learning applications, marked by limited observable events and significant observational bias favoring high-significance bursts—two longstanding limitations that our physics-informed data augmentation framework directly overcomes.

By generating over 100,000 synthetic GRB samples that an order-of-magnitude expansion from the original 6,189 real-world observations, this framework effectively mitigates observational selection bias against low-significance events and resolves the "observational iceberg" effect described by Lü et al. (2014) and Moss et al. (2022), where the majority of astrophysical transients lie below conventional detection thresholds due to instrumental sensitivity limitations and background contamination.

As demonstrated in Figure 2, our methodology successfully **reduces** the observational bias against low-significance events, which constitute the predominant population of actual GRB phenomena yet remain systematically underrepresented in existing catalogs. Specifically, we bin light curves into 9 distinct energy channels following traditional trigger search algorithms (von Kienlin et al. 2020; Cai et al. 2021), preserving crucial spectral information while enhancing signal detectability. We then systematically modulate burst SNR while retaining realistic background characteristics, yielding physically faithful synthetic samples that span the full dynamic range of actual GRB phenomena. This approach not only reduces model overfitting but also enhances sensitivity to weak transients—critical for capturing the majority of GRBs that lie below conventional detection thresholds due to instrumental constraints. The proposed augmentation framework offers substantial advantages for GRB identification systems by **alleviating** several fundamental limitations in current approaches. Furthermore, the enhanced sample diversity allows the development of detection algorithms with improved sensitivity to weak transients that typically evade identification in standard analysis pipelines. As such, the augmentation strategy provides a generalizable solution for transient astronomy, where limited mission durations and observational biases often hinder deep learning applications.

We design a novel Adaptive Frequency Feature Enhancement module, AFFE, which represents a methodological advance in addressing the spectral-temporal complexity of GRB signals. Unlike conventional time-domain attention mechanisms (e.g., SE, CBAM, ECA) that fail to capture frequency-domain correlations, or fixed-frequency filters lacking adaptability, AFFE employs a dual-path architecture to perform data-driven spectral weighting—enabling adaptive soft-threshold denoising and coherent feature extraction without manual filter design. This mechanism aligns with the complex, variable frequency signatures of GRBs, optimizing the model's ability to distinguish GRBs from non-GRB signals by leveraging discriminative frequency components. Integrating AFFE with a ResNet baseline yields a classification accuracy of 97.46%, representing a statistically significant 3% improvement over the state-of-the-art 2D ResNet-CBAM architecture (94.46%; (Zhang et al. 2024)). Comparative analysis of these models and their predictive uncertainty reveal that our AFFE implementation shows superior performance metrics, establishing a new benchmark for high-precision GRB identification. Comparative analysis further validates that this frequency-adaptive architecture maintains performance advantages even near theoretical accuracy saturation, demonstrating its superiority and robustness in handling the unique spectral dynamics of GRB light curves.

Further validation confirms that this frequency-adaptive architecture maintains performance advantages even near theoretical accuracy saturation, demonstrating its superiority and robustness in handling the unique spectral dynam-

ics of GRB light curves, highlighting the methodological advancement in alleviating the unique challenges of GRB identification. As visualized in Figure 4, the model selectively attends to critical burst characteristics, exhibiting strong concordance with domain expertise in GRB identification. The incorporation of the AFFE module significantly enhances the ResNet architecture's capacity to extract physically meaningful features, enabling comprehensive characterization of burst processes. This Fourier-domain enhancement improves classification by explicitly modeling spectral-temporal correlations—critical for distinguishing GRBs from noise, as key burst signatures (e.g., multi-phase emission, spectral lags) are jointly encoded in both time and frequency domains. It is important to note that predictive uncertainty remains a critical consideration in real-world astrophysical applications. while our model achieves high accuracy, the confidence of predictions—especially for low-significance or atypical bursts—requires further quantification, and future work should integrate uncertainty estimation techniques to better assess classification reliability.

Additionally, Grad-CAM feature visualization and UMAP dimensionality reduction confirm the model's ability to focus on physically meaningful T_{90} regions and reveal intrinsic clustering of GRBs by origin, morphology, and observational properties (SNR, duration). The geometric structure of the low-dimensional UMAP embedding reflects the model's success in capturing fundamental physical differences between GRB subclasses. Misclassified GRBs are predominantly located in low-SNR regions, suggesting that these faint detections require specialized further analysis. The model exhibits clear distribution differences between long and short bursts, confirming its ability to capture discriminative features for GRB classification and successfully capture subtle variations in light curve morphology and temporal evolution patterns.

We also gain valuable physical insights from model-derived features. The dimensionality reduction and AutoGMM clustering of model-extracted features uncover meaningful physical patterns in GRB populations. Kilonova-associated GRBs (GRB-KN) predominantly cluster in Clusters 2 and 3, with long-duration GRB-KN in Cluster 2 sharing multi-phase light curve morphologies—supporting a common progenitor system as proposed by previous theoretical work (Zhu et al. 2022), suggesting a common progenitor system for these apparently long-duration events. A particularly compelling case is presented by GRB 211211A and GRB 230307A, which exhibit nearly identical three-phase emission structures (precursor, main burst, extended emission) and occupy adjacent regions in the low-dimensional embedding space (Dimple et al. 2023; Negro et al. 2025). The comprehensive temporal and spectral analyses of their strikingly similar properties indicate a common mechanism (Peng et al. 2024; Wang et al. 2025). This clustering pattern mirrors yet remains distinct from the tight grouping of GRB-SN in Clusters 1 and 2, which similarly reflects their shared progenitor physics (Kumar & Sharma 2024; Kumar 2025). GRBs with extended emission show spatial separation into three subgroups highly correlated with duration, while ultra-long GRBs are confined to the lGRB-dominated Cluster 3—hinting at potential subclasses with physical origins independent of standard duration-based classification. Notably, sGRBs with precursors occupy transitional zones between short and long GRB clusters, indicating hybrid characteristics and diverse progenitor systems. In contrast, lGRBs with precursors show widespread dispersion, implying precursor activity is an independent physical process rather than a core burst characteristic. These findings reinforce the limitations of duration-only GRB classification, aligning with prior studies (e.g., (Modak 2021)) that highlight inherent uncertainties in this paradigm. The model's ability to aggregate GRBs by physical origin rather than just observational parameters demonstrates that machine learning-derived features can serve as a complementary dimension for probing GRB progenitors, with future increases in the sample size of events with confirmed origins essential for further validating these classification schemes.

Despite achieving high classification accuracy, the model exhibits residual misclassification of low-SNR GRBs (99% of false negatives have peak-SNR $< 5\ \sigma$), which may require specialized feature engineering or multi-modal data integration (e.g., combining light curves with spectral data, energy response-corrected data) for further improvement. Predictive uncertainty quantification—critical for real-world astrophysical applications—also warrants deeper integration, as confidence assessment for low-significance or atypical bursts remains underdeveloped. Additionally, validating the clustering results for special GRB subclasses (e.g., GRB-KN, precursor-containing GRBs) requires larger samples of events with confirmed origins. Future work will focus on three key directions: (1) integrating Monte Carlo Dropout or Bayesian neural networks to quantify prediction uncertainty and improve reliability for faint events; (2) expanding the framework to process multi-modal data (spectral, temporal, and polarization information) for richer feature extraction; (3) adapting the model for real-time analysis pipelines in time-domain and multi-messenger astronomy, enabling faster detection and characterization of transient phenomena. The adaptive frequency-domain approach and data augmentation strategy developed here are also generalizable to other transient astrophysical events (e.g., fast

radio bursts, soft gamma-ray repeaters, supernovae), highlighting their broader potential for advancing observational capabilities.

In summary, this study advances GRB identification through a synergistic combination of physics-informed data augmentation and frequency-adaptive feature enhancement, effectively addressing core challenges of limited training samples, observational selection bias, and inadequate discriminative feature extraction in GRB studies. By generating over 100,000 physically faithful pseudo-GRB samples, via our augmentation strategy, we effectively mitigate data scarcity, alleviate the "observational iceberg" effect, and substantially enhance the model's generalization capability to faint, low-significance bursts. We further elevate detection performance by developing a ResNet-based deep learning framework integrated with the novel AFFE module, which adaptively weights and filters frequency-domain components to capture key GRB signatures. The framework not only achieves high classification accuracy that outperforming conventional attention mechanisms and frequency-domain approaches, but also provides actionable physical insights into GRB populations by capturing intrinsic relationships between observational signatures and progenitor origins. Through feature visualization and dimensionality reduction, we demonstrate that GRBs aggregated in the model's feature space share similar physical attributes, highlighting that machine learning-derived features offer an additional dimension for probing GRB origins beyond traditional duration-based classification paradigms. We emphasize the broad potential of adaptive frequency-domain analysis for advancing GRB identification and underscore the generalizability of our approach to other transient astronomical phenomena. As time-domain and multi-messenger astronomy rapidly evolve, there is an urgent demand for higher accuracy, improved temporal resolution, and the ability to uncover latent feature relationships. Future work will integrate generalized machine learning models capable of processing multi-band and multi-modal data into real-time analysis pipelines—enabling deeper feature extraction, faster transient detection, and more precise characterization—thereby laying the groundwork for robust transient detection systems that leverage the growing volume of data from next-generation astronomical missions.

6. ACKNOWLEDGEMENTS

The code and data sets are available upon reasonable request.

REFERENCES

Abraham, S., Mukund, N., Vibhute, A., et al. 2021, MNRAS, 504, 3084, doi: 10.1093/mnras/stab1082

Alzubaidi, L., Zhang, J., Humaidi, A. J., et al. 2021, Journal of Big Data, 8. https://api.semanticscholar.org/CorpusID:232434552

Athey, T. L., Liu, T., Pedigo, B. D., & Vogelstein, J. T. 2019, arXiv e-prints, arXiv:1909.02688, doi: 10.48550/arXiv.1909.02688

Band, D. L. 2002, ApJ, 578, 806, doi: 10.1086/342661

Basora, L., Viens, A., Chao, M. A., & Olive, X. 2025, Reliability Engineering & System Safety, 253, 110513, doi: https://doi.org/10.1016/j.ress.2024.110513

Blackburn, L., Briggs, M. S., Camp, J., et al. 2013, arXiv e-prints, arXiv:1303.2174, doi: 10.48550/arXiv.1303.2174

Cai, C., Xiong, S. L., Li, C. K., et al. 2021, MNRAS, 508, 3910, doi: 10.1093/mnras/stab2760

Chen, J.-M., Zhu, K.-R., Peng, Z.-Y., & Zhang, L. 2024, MNRAS, 527, 4272, doi: 10.1093/mnras/stad3407

—. 2025, ApJS, 276, 62, doi: 10.3847/1538-4365/ada0b0

Coppin, P., de Vries, K. D., & van Eijndhoven, N. 2020, PhRvD, 102, 103014, doi: 10.1103/PhysRevD.102.103014

Crupi, R., Dilillo, G., Bissaldi, E., et al. 2023, Experimental Astronomy, 56, 421, doi: 10.1007/s10686-023-09915-7

Deng, H.-Y., Peng, Z.-Y., Chen, J.-M., & Zhu, D. 2024, Research in Astronomy and Astrophysics, 24, 035013, doi: 10.1088/1674-4527/ad0497

Dimple, Misra, K., & Arun, K. G. 2023, ApJL, 949, L22, doi: 10.3847/2041-8213/acd4c4

Eldele, E., Ragab, M., Chen, Z., Wu, M., & Li, X. 2024, arXiv e-prints, arXiv:2404.08472, doi: 10.48550/arXiv.2404.08472

Finneran, G., Cotter, L., & Martin-Carrillo, A. 2024, arXiv
  e-prints, arXiv:2411.08866,
  doi: 10.48550/arXiv.2411.08866

Gal, Y., & Ghahramani, Z. 2015, arXiv e-prints,
  arXiv:1506.02142, doi: 10.48550/arXiv.1506.02142

Garcia-Cifuentes, K., Becerra, R. L., De Colle, F., Cabrera,
  J. I., & Del Burgo, C. 2023, ApJ, 951, 4,
  doi: 10.3847/1538-4357/acd176

Guidorzi, C., Dichiara, S., & Amati, L. 2016, A&A, 589,
  A98, doi: 10.1051/0004-6361/201527642

He, K., Zhang, X., Ren, S., & Sun, J. 2015, in Proceedings
  of the 2015 IEEE International Conference on Computer
  Vision (ICCV), ICCV '15 (USA: IEEE Computer
  Society), 1026–1034, doi: 10.1109/ICCV.2015.123

He, K., Zhang, X., Ren, S., & Sun, J. 2016, in Proceedings
  of 2016 IEEE Conference on Computer Vision and
  Pattern Recognition, CVPR '16 (IEEE), 770–778,
  doi: 10.1109/CVPR.2016.90

Hu, J., Shen, L., & Sun, G. 2018, in 2018 IEEE/CVF
  CONFERENCE ON COMPUTER VISION AND
  PATTERN RECOGNITION (CVPR), IEEE Conference
  on Computer Vision and Pattern Recognition, IEEE;
  CVF; IEEE Comp Soc, 7132–7141,
  doi: 10.1109/CVPR.2018.00745

Jespersen, C. K., Severin, J. B., Steinhardt, C. L., et al.
  2020, ApJL, 896, L20, doi: 10.3847/2041-8213/ab964d

Kingma, D. P., & Ba, J. 2014, arXiv e-prints,
  arXiv:1412.6980, doi: 10.48550/arXiv.1412.6980

Kumar, A. 2025, NewA, 116, 102346,
  doi: 10.1016/j.newast.2024.102346

Kumar, A., & Sharma, K. 2024, arXiv e-prints,
  arXiv:2411.13242, doi: 10.48550/arXiv.2411.13242

Kumar, P., & Zhang, B. 2015, PhR, 561, 1,
  doi: 10.1016/j.physrep.2014.09.008

Li, Q. M., Sun, Q. B., Zhang, Z. B., Zhang, K. J., & Long,
  G. 2024, MNRAS, 527, 7111,
  doi: 10.1093/mnras/stad3619

Li, Q. M., Zhang, Z. B., Han, X. L., et al. 2023, MNRAS,
  524, 1096, doi: 10.1093/mnras/stad1648

Liu, M., Zeng, A., Lai, Q., & Xu, Q. 2020, T-WaveNet:
  Tree-Structured Wavelet Neural Network for
  Sensor-Based Time Series Analysis.
  https://arxiv.org/abs/2012.05456

Liu, P., Wu, B., Li, N., et al. 2024, in ICASSP 2024 - 2024
  IEEE International Conference on Acoustics, Speech and
  Signal Processing (ICASSP), 5960–5964,
  doi: 10.1109/ICASSP48485.2024.10446883

Lü, H.-J., Liang, E.-W., Zhang, B.-B., & Zhang, B. 2010,
  ApJ, 725, 1965, doi: 10.1088/0004-637X/725/2/1965

Lü, H.-J., Zhang, B., Liang, E.-W., Zhang, B.-B., &
  Sakamoto, T. 2014, MNRAS, 442, 1922,
  doi: 10.1093/mnras/stu982

Ma, P. X., Ng, C., Rizk, L., et al. 2023, Nature Astronomy,
  7, 492, doi: 10.1038/s41550-022-01872-z

Margutti, R., & Chornock, R. 2021, ARA&A, 59, 155,
  doi: 10.1146/annurev-astro-112420-030742

Mészáros, P. 2019, MmSAI, 90, 57.
  https://arxiv.org/abs/1904.10488

Modak, S. 2021, Astronomy and Computing, 34, 100441,
  doi: 10.1016/j.ascom.2020.100441

Moss, M., Lien, A., Guiriec, S., Cenko, S. B., & Sakamoto,
  T. 2022, ApJ, 927, 157, doi: 10.3847/1538-4357/ac4d94

Negro, M., Cibrario, N., Burns, E., et al. 2025, ApJ, 981,
  14, doi: 10.3847/1538-4357/ada8a9

Nemani, V., Biggio, L., Huan, X., et al. 2023, Mechanical
  Systems and Signal Processing, 205, 110796,
  doi: 10.1016/j.ymssp.2023.110796

Parmiggiani, N., Bulgarelli, A., Fioretti, V., et al. 2021,
  APJ, 914, 67, doi: 10.3847/1538-4357/abfa15

Parmiggiani, N., Bulgarelli, A., Ursi, A., et al. 2023, APJ,
  945, 106, doi: 10.3847/1538-4357/acba0a

Parmiggiani, N., Bulgarelli, A., Macaluso, A., et al. 2024,
  arXiv e-prints, arXiv:2404.02107,
  doi: 10.48550/arXiv.2404.02107

Pe'er, A. 2024, Galaxies, 13, 2,
  doi: 10.3390/galaxies13010002

Peng, Z.-Y., Chen, J.-M., & Mao, J. 2024, ApJ, 969, 26,
  doi: 10.3847/1538-4357/ad45fc

Ror, A. K., Gupta, R., Aryan, A., et al. 2024, ApJ, 971,
  163, doi: 10.3847/1538-4357/ad5554

Rudolph, A., Petropoulou, M., Winter, W., & Bošnjak, Ž.
  2023, ApJL, 944, L34, doi: 10.3847/2041-8213/acb6d7

Selvaraju, R. R., Cogswell, M., Das, A., et al. 2017, in 2017
  IEEE International Conference on Computer Vision
  (ICCV), Venice, Italy, 618–626,
  doi: 10.1109/ICCV.2017.74

Shorten, C., & Khoshgoftaar, T. M. 2019, JOURNAL OF
  BIG DATA, 6, doi: 10.1186/s40537-019-0197-0

Sun, H., Wang, C. W., Yang, J., et al. 2023, arXiv e-prints,
  arXiv:2307.05689, doi: 10.48550/arXiv.2307.05689

Tarnopolski, M., & Marchenko, V. 2021, ApJ, 911, 20,
  doi: 10.3847/1538-4357/abe5b1

Taye, M. M. 2023, computation, 11, 52,
  doi: 10.3390/computation11030052

von Kienlin, A., Meegan, C. A., Paciesas, W. S., et al. 2020,
  ApJ, 893, 46, doi: 10.3847/1538-4357/ab7a18

Wang, C.-W., Tan, W.-J., Xiong, S.-L., et al. 2024, arXiv
  e-prints, arXiv:2407.02376,
  doi: 10.48550/arXiv.2407.02376

—. 2025, ApJ, 979, 73, doi: 10.3847/1538-4357/ad98ec

Wang, J.-S., Peng, Z.-K., Zou, J.-H., Zhang, B.-B., & Zhang, B. 2020, ApJL, 902, L42, doi: 10.3847/2041-8213/abbfb8

Wang, Q., Wu, B., Zhu, P., et al. 2020, in 2020 IEEE/CVF CONFERENCE ON COMPUTER VISION AND PATTERN RECOGNITION (CVPR 2020), IEEE Conference on Computer Vision and Pattern Recognition, IEEE; CVF; IEEE Comp Soc, 11531–11539, doi: 10.1109/CVPR42600.2020.01155

Woo, S., Park, J., Lee, J.-Y., & Kweon, I. S. 2018, in Computer Vision – ECCV 2018, ed. V. Ferrari, M. Hebert, C. Sminchisescu, & Y. Weiss (Cham: Springer International Publishing), 3–19, doi: 10.1007/978-3-030-01234-2_1

Wu, H., Hu, T., Liu, Y., et al. 2022, arXiv e-prints, arXiv:2210.02186, doi: 10.48550/arXiv.2210.02186

Zhang, B. 2011, Comptes Rendus Physique, 12, 206, doi: 10.1016/j.crhy.2011.03.004

Zhang, P., Li, B., Gui, R., et al. 2024, ApJS, 272, 4, doi: 10.3847/1538-4365/ad2de5

Zhang, S., Shao, L., Zhang, B.-B., et al. 2022, ApJ, 926, 170, doi: 10.3847/1538-4357/ac4753

Zhong, S.-Q., Dai, Z.-G., Cheng, J.-G., Lan, L., & Zhang, H.-M. 2019, ApJ, 884, 25, doi: 10.3847/1538-4357/ab3e48

Zhou, T., Ma, Z., Wen, Q., et al. 2022, arXiv e-prints, arXiv:2201.12740, doi: 10.48550/arXiv.2201.12740

Zhou, Z.-M., Wang, X.-G., Liang, E.-W., et al. 2024, ApJ, 972, 190, doi: 10.3847/1538-4357/ad5f90

Zhu, J.-P., Wang, X. I., Sun, H., et al. 2022, ApJL, 936, L10, doi: 10.3847/2041-8213/ac85ad

Zhu, S.-Y., Sun, W.-P., Ma, D.-L., & Zhang, F.-W. 2024, MNRAS, 532, 1434, doi: 10.1093/mnras/stae1594